PHYSICAL REVIEW E VOLUME 62, NUMBER 3 SEPTEMBER 2000

Instability of symmetric Couette flow in a granular gas: Hydrodynamic field profiles and transport

M. Sasvári,[1,2] J. Kertész,[1] and D. E. Wolf[2]
[1]Department of Theoretical Physics, Technical University of Budapest, Budafoki út 8, H-1111 Hungary
[2] University Duisburg, D-45478 Duisburg, Germany

(Received 22 March 2000)

We investigated the inelastic hard-disk gas sheared by two parallel bumpy walls (Couette flow). In our molecular dynamic simulations we found a sensitivity to the asymmetries of the initial particle positions and velocities and an asymmetric stationary state, where the deviation from (anti)symmetric hydrodynamic fields is stronger as the normal restitution coefficient decreases. For better understanding of this sensitivity we carried out a linear stability analysis of the former kinetic theoretical solution [J. T. Jenkins and M. W. Richman, J. Fluid. Mech. **171**, 53 (1986)] and found it to be unstable. The effect of this asymmetry on the self-diffusion coefficient is also discussed.

PACS number(s): 45.70.Mg, 45.70.Qj, 51.10.+y, 51.20.+d

I. INTRODUCTION

In the last decade the clustering instability of undriven granular gases has been extensively researched. Since the first explanation of the instability [1], investigations have been made by several methods including stability analysis of the hydrodynamic equations [2,3] and fluctuating hydrodynamics [4]. The influence of nonlinear coupling between hydrodynamic modes has also been studied [5], and the long time behavior of the clustered state examined with mode-coupling theories [6]. The evolution of vortex velocity patterns preceding the clustering instability is well understood [4], and the minimal system size, where the instability appears and its dependence on the restitution coefficient have been found [5,7].

A driven configuration, the uniformly sheared inelastic hard-sphere gas (with periodic boundary conditions) also shows an instability and resulting pattern formation. In [8] it was shown that this pattern formation is guided by an instability for short times and a shearing-caused convection for longer time scales. The special importance of this system is the coupling of macroscopic and microscopic length scales in sheared situations, as discussed in [9–11].

A more realistic configuration is Couette flow, the shearing of the gas between two parallel walls moved in opposite directions. For this configuration with walls consisting of disks Jenkins and Richman derived boundary conditions for the momentum and heat transfer of the walls [12], proceeding from their kinetic theory for dense granular gases [13]. In subsequent years this theory was developed further [14] for non-Maxwellian velocity distributions as in [12]. In all of these papers the resulting hydrodynamic fields are symmetric (density and granular temperature) or antisymmetric (flow field) around the halfway point between the two bounding walls. It is of major interest whether the clustering instability occurs in this configuration also and, if so, what its consequences are in the Couette flow. This paper is devoted to the investigation of these questions.

The paper is organized as follows. In Sec. II we present molecular dynamic simulations of this system, where we found an interesting sensitivity to the initial conditions of the simulation and asymmetric hydrodynamic fields, contradicting the results in [12]. Therefore we carried out a linear stability analysis (Sec. III) around the solution of Jenkins and Richman [12] and found it to be unstable against certain fluctuations. We discuss the effect of this instability on the diffusion coefficient in Sec. IV and close the paper with a discussion in Sec. V.

II. SIMULATION RESULTS

The system considered here consisted of N identical, inelastic hard disks with mass $m=1$ and radius $r=1$ confined in a rectangular area of size $L_x \times L_y$. This two-dimensional area is bounded by parallel walls on two sides, which also define the direction x and are of length L_x. The system is closed through periodic boundary conditions in the x direction. The walls are L_y distance apart (y direction). The origin of the coordinate system is placed in the middle of the simulated system, which sets the center of the wall disks at $y = \pm L_y/2$.

The disks interact through an inelastic rough hard-sphere potential, meaning that instantaneous two-particle collisions occur characterized by ratios of the final and initial velocities in the normal and tangential directions given by the normal and tangential restitution coefficients $e_n = -v_n^f/v_n^i$ and $e_t = v_t^f/v_t^i$, f and i meaning the final and initial velocities. In case of sliding contacts e_t is replaced by the ratio of tangential and normal momentum transfer characterized by the friction coefficient μ. As a driving force we move one of the walls with constant velocity $2U$.

We investigated the system with the event-driven molecular dynamics method ideal for simulating instantaneous collision rules [15]. To characterize the collisions we used $e_t = -0.3$ and $\mu = 0.2$ and varied e_n between 0.6 and 0.99. We consider the system size $L_x = L_y = 40$ and the wall velocity $2U = 10$ if not otherwise mentioned. The post collision velocities and angular velocities as functions of the precollision values are (for $m=1$, $r=1$)

1063-651X/2000/62(3)/3817(9)/$15.00

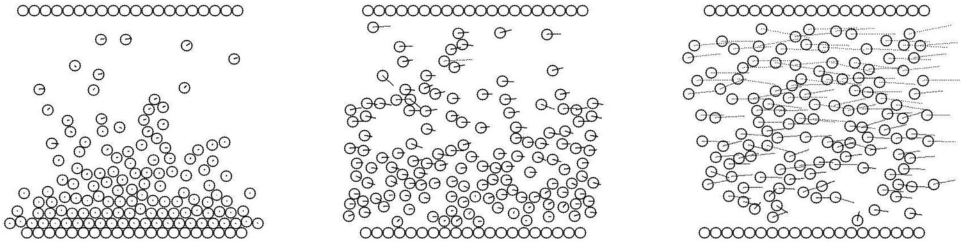

FIG. 1. Snapshot configurations in the steady state for different restitution coefficients $e_n=0.7$, 0.8, 0.9 from left to right. Lines from centers of particles indicate the direction and magnitude of its velocity.

$$\mathbf{v}_i' = \mathbf{v}_i - \frac{1+e_n}{2}[(\mathbf{v}_i-\mathbf{v}_j)\mathbf{r}_n]\mathbf{r}_n + \frac{j_t}{m}\mathbf{r}_t, \tag{1}$$

$$\mathbf{v}_j' = \mathbf{v}_j + \frac{1+e_n}{2}[(\mathbf{v}_i-\mathbf{v}_j)\mathbf{r}_n]\mathbf{r}_n + \frac{j_t}{m}\mathbf{r}_t, \tag{2}$$

$$\boldsymbol{\omega}_i' = \boldsymbol{\omega}_i - \frac{j_t}{I_i}(\mathbf{r}_n \times \mathbf{r}_t), \tag{3}$$

$$\boldsymbol{\omega}_j' = \boldsymbol{\omega}_i - \frac{j_t}{I_j}(\mathbf{r}_n \times \mathbf{r}_t). \tag{4}$$

$\mathbf{r}_n$ is the normal vector of disk surfaces in collision $\mathbf{r}_n=(\mathbf{r}_j-\mathbf{r}_i)/|\mathbf{r}_j-\mathbf{r}_i|$ and $\mathbf{r}_t$ the tangential vector, the normal vector rotated by $\pi/2$ in the counterclockwise direction. I_i and I_j are the moments of inertia of the disks. The parameter j_t depends on the type of collision in the tangential direction,

$$j_t = -\mu\frac{1+e_n}{2}(\mathbf{v}_i-\mathbf{v}_j)\mathbf{r}_n \quad \text{if} \quad \phi > \phi_0 \quad (\text{sliding contact}), \tag{5}$$

$$j_t = \frac{e_t-1}{7}\mathbf{v}_t \quad \text{if} \quad \phi \leqslant \phi_0 \quad (\text{sticking contact}), \tag{6}$$

where $\mathbf{v}_t$ is the tangential velocity

$$\mathbf{v}_t = (\mathbf{v}_i-\mathbf{v}_j)\mathbf{r}_t + r(\boldsymbol{\omega}_j+\boldsymbol{\omega}_j) \tag{7}$$

and ϕ_0 separates the sliding and sticking regions in terms of the angle of incidence $\phi=|\mathbf{v}_t|/[(\mathbf{v}_i-\mathbf{v}_j)\mathbf{r}_n]$,

$$\phi_0 = \frac{7}{2}\mu\frac{1+e_n}{1-e_t}. \tag{8}$$

To avoid inelastic collapse [16], the intrinsic numerical breakdown of the method, we stopped the simulations when the time interval between two subsequent collisions became smaller than the precision of the computations proposed in [1]; but this stop occurred only for the smallest restitution coefficient used $e_n=0.6$, and for special initial conditions where most of the particles did not move and the well-known chainlike arrangement of particles could evolve after the simulation started. For the experiments below we used particle numbers $N=100$–240, meaning area fraction $\nu\in[0.245,0.49]$. As test runs for larger systems we used $\{L_x=L_y=100,\ N=500,\ (\overline{\nu}=0.162)\}$ and $\{L_x=L_y=100,\ N=1000,\ (\overline{\nu}=0.324)\}$ parameter sets, resulting in the same phenomenon.

Using several different starting configurations we noted that a dense region appears at one of the walls in the system which becomes more and more distinct with decreasing e_n, but is not recognizable for e_n near 1 (Fig. 1). Using randomly placed particles and an initial uniform velocity distribution with several mean values in the x direction, we observed that the initial value of the mean particle velocity determines the wall that is chosen for building up a clustered regime. If we define v_d as

$$v_d = \langle v\rangle - U,$$

we can characterize the final position: if $v_d>0$ the upper wall $y=L_y/2$ is chosen; if $v_d<0$ the lower wall $y=-L_y/2$ (Fig. 2). We used different initial conditions to test this finding [17]. With particles placed in a stripe in the middle of the system, organized on a lattice with initial velocity U, and using two of them shot against the two walls with initial velocities that were Galileo symmetric with the situation of two walls moving at $\pm U$, we could maximize the time needed to develop the nonsymmetric density field, but it eventually appeared after these initial conditions also, because numerical errors provide the needed fluctuations to drive the system into one of the steady states.

We did simulations for smooth disks ($e_t=1$ and $\mu=0$) also and found the same effect, namely, if we choose e_n to be small enough there is a distinct band of particles at one of the walls and for e_n close to 1 this band does not evolve. The normal restitution below which we can speak about an asymmetric phase depends on the density; for higher densities it appears at higher e_n values for the same system size L_y. It also depends on L_y for fixed density; for larger L_y the kinetic energy influx per particle decreases as it is proportional to the length of the wall. The assumed critical restitution coefficient $e_c(\rho,L_y)$ does not depend on the driving velocity as U is the only parameter that includes the dimensionality of time and changing U is a rescaling of the time unit. For investigation of intermediate e_n values for which the dense stripe is not so definite, we measured density and velocity profiles

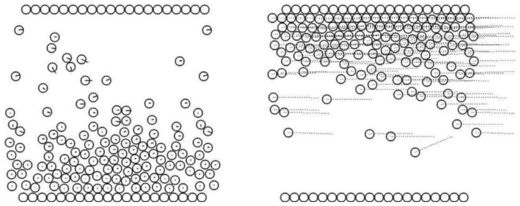

FIG. 2. Snapshot configurations in the steady state for different initial velocity distributions ($e_n=0.7$). Left, $v_d<0$; right, $v_d>0$.

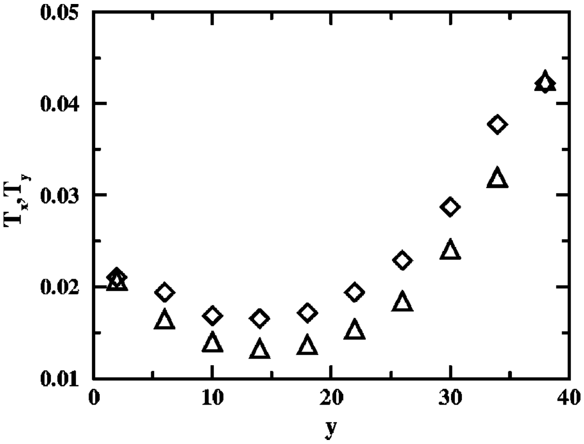

FIG. 3. Granular temperature in the x and y directions as a function of y (in units of disk radius $r=1$) across the system for $e_n=0.9$. Values are averages over stripes of width 4 parallel to the walls for a system of size $L_y=40$.

and the granular temperature in the system and found the same effect in the asymmetric nature of these functions (Fig. 3). One can observe that with decreasing restitution the minimum of the granular temperature moves to one of the walls.

We found these results to be valid for a broad range of densities and for different system sizes. For low restitution a crystalline structure appeared as compact layers near a wall. The fact that the simulations did not stop at such dense configurations implies that the disks moved around a fixed place and did not form a connected line of particles long enough for inelastic collapse to occur [16].

Simulations with time-step-driven molecular dynamics using damped harmonic oscillator forces between the particles as a function of their overlap [15]—to achieve velocity independent restitution—show the same clustering effect at the walls. This suggests that this effect is closely related to dissipative collisions and does not require instantaneous collision rules.

III. STABILITY OF THE JENKINS-RICHMAN SOLUTION

Our findings above contradict the kinetic theoretical calculation of Jenkins and Richman [12] and the improved versions of the problem [14], inasmuch as the cited results are always (anti)symmetric profiles in the y direction for the hydrodynamic fields of density, flow velocity, and granular temperature. This contradiction raises the question of the stability of the (anti)symmetric solution. Moreover, it is plausible that in an elastic system the hydrodynamic profiles will be symmetric, although this is not a steady state because of the ever rising temperature caused by viscous heating. Therefore, it is of interest to see whether a phase transition occurs in the system; specifically, whether there exists a critical e_n value separating the (anti)symmetric and asymmetric phases or the (anti)symmetric solution is unstable at arbitrarily small inelasticities. Because at high densities the instability in question arises at normal restitution closer to 1 and kinetic theoretical calculations are more and more inadequate for increasing inelasticity, it is reasonable to use kinetic theories for dense systems and we desist from the consideration of more sophisticated hydrodynamic equations for low density systems [18,19]. Another reason for taking theories for dense gases into consideration is that the underlying assumptions are more valid as the ratio of the simulated system size to the mean free path is much larger in a dense gas. For these reasons we performed a linear stability analysis of the Jenkins-Richman solution. We now first give the equations of Jenkins and Richman [13] and the boundary conditions and the solution of the problem [12]. Then we perform a linearization around this solution and calculate numerically the eigenvalues of the stability matrix.

A. Jenkins-Richman solution

In this section we briefly describe the Jenkins and Richman [12] solution for a two-dimensional system of inelastic hard disks driven by two parallel bumpy walls. The hydrodynamic equations for the density ρ, flow velocity $\mathbf{u}$, and fluctuation energy T for smooth disks without external forces are (see [13])

$$\dot{\rho}=-\rho\boldsymbol{\nabla}\cdot\mathbf{u}, \tag{9}$$

$$\rho\dot{\mathbf{u}}=-\boldsymbol{\nabla}\cdot\mathbf{P}, \tag{10}$$

$$\rho\dot{T}=-\boldsymbol{\nabla}\cdot\mathbf{Q}-\mathrm{Tr}(\mathbf{P}\cdot\boldsymbol{\nabla}\mathbf{u})-\gamma. \tag{11}$$

Here the dissipation rate γ and heat transport coefficient κ are of the form

$$\gamma=\frac{4(1-e_n)\kappa T}{\sigma^2}, \tag{12}$$

$$\kappa=\frac{2\rho\sigma\nu g_0 T^{1/2}}{\pi^{1/2}}, \tag{13}$$

where g_0 is the Enskog correction term accounting for excluded volume effects as a function of the packing fraction ν,

$$g_0=\frac{16-7\nu}{16(1-\nu)^2},$$

and $\sigma=2r$ is the disk diameter. The constitutive relations for the energy flux $\mathbf{Q}$ and pressure tensor $\mathbf{P}$ are

$$\mathbf{Q}=-\kappa\boldsymbol{\nabla}T, \tag{14}$$

$$\mathbf{P}=\left[2\rho\nu g_0 T-\frac{1}{2}\kappa\,\mathrm{Tr}(\mathbf{D})\right]\mathbf{I}-\kappa\mathbf{D}. \tag{15}$$

From the boundary geometry and the assumption of a Maxwellian velocity distribution the momentum and fluctuation energy supplied by the wall in unit time and length are determinable [12]. This needs an expansion in $\epsilon=\sigma/L_y$ and assumptions about the dependence of given ratios of the hydrodynamic fields on ϵ (see [12]), which narrows the validity of the theory. The supplied momentum obtained in that way is

$$M_\alpha=\frac{1}{2}\rho\chi(1+e_n)T\left[n_\alpha+\left(\frac{2}{\pi}\right)^{1/2}\frac{v_\alpha}{T^{1/2}}\left(\frac{\theta}{\sin\theta}-\cos\theta\right)\right.$$
$$\left.+\left(\frac{2}{\pi}\right)^{1/2}\frac{\sigma}{T^{1/2}}u_{\gamma,\beta}I_{\alpha\beta\gamma}\right] \qquad (16)$$

with

$$I_{\alpha\beta\gamma}=\left(\frac{2}{3}\sin^2\theta-2\right)n_\alpha n_\beta n_\gamma$$
$$-\frac{2}{3}\sin^2\theta(n_\alpha t_\beta t_\gamma+n_\beta t_\alpha t_\gamma+n_\gamma t_\alpha t_\beta), \qquad (17)$$

and the supplied fluctuation energy is

$$D=\left(\frac{2}{\pi}\right)^{1/2}\frac{\rho\chi(1-e_n)T^{3/2}}{\sin\theta}, \qquad (18)$$

where **n** and **t** are the normal and tangential vectors of the wall, respectively, and θ characterizes the bumpiness of the wall. For wall disks with the same diameter as that of the gas particles, θ is given by [12]

$$\sin\theta=\frac{\sigma}{d},$$

where d is the distance separating the centers of two wall disks. For the wall geometry of our system, $d=2\sigma$ and therefore $\sin\theta=1/2$ and $\theta=\pi/6$. In Eqs. (16) and (18) χ accounts for static correlation effects in collisions at the boundary and v_α, $\alpha=x,y$ is the slip velocity, the difference between the velocity of the wall and the flow, $\mathbf{v}=\mathbf{U}-\mathbf{u}$. From the equality of momentum and energy transfer of the wall for unit time and unit length the boundary conditions are

$$\mathbf{M}=\mathbf{P}\cdot\mathbf{n}, \qquad (19)$$

$$\mathbf{M}\cdot\mathbf{v}-D=\mathbf{Q}\cdot\mathbf{n}. \qquad (20)$$

The solution can be calculated from these equations except for one parameter—the value of the solid fraction at the boundaries (for fixed number of particles)—which must be iterated to get the given density in the system, which we did numerically. Thus the form of the hydrodynamic fields solving the boundary value problem is

$$w(y)=\frac{\lambda(U-v)N\sigma}{2\pi^{1/2}\sinh(\lambda/2)SL}\cosh\left(\frac{\lambda y}{L}\right), \qquad (21)$$

$$u(y)=\frac{U-v}{\sinh(\lambda/2)}\sinh\left(\frac{\lambda y}{L}\right) \qquad (22)$$

with $T(y)=w(y)^2$, S and N are the shear stress and pressure, respectively, and λ must be solved from [12]

$$\frac{\lambda}{2}\tanh\left(\frac{\lambda}{2}\right)=\frac{(1-e_n)L\theta}{2\sqrt{2}\sigma\sin\theta}\left(\frac{\sin\theta[1-(4\sqrt{2}/3)\sin^2\theta]}{\theta(\theta/\sin\theta-\cos\theta)}-1\right). \qquad (23)$$

The density, calculated from

$$\chi=2\nu g_0, \qquad (24)$$

must fulfill the condition that its integral on the whole system gives the prepared particle number. As mentioned, in that condition the only free parameter remaining is the density at the boundaries, which must be calculated iteratively.

B. Stability analysis

Around the above solution of the boundary value problem we performed a linear stability analysis with the perturbed quantities

$$\rho'=\rho+\delta\rho, \qquad (25)$$

$$\mathbf{u}'=\mathbf{u}+\delta\mathbf{u}, \qquad (26)$$

$$T'=T+\delta T. \qquad (27)$$

We split the velocity perturbation in the x and y directions and use plane waves for the perturbations,

$$\delta\rho=\delta\rho_{\mathbf{k}}\exp(-i\mathbf{k}\cdot\mathbf{r}), \qquad (28)$$

$$\begin{pmatrix}\delta u\\ \delta w\end{pmatrix}=\begin{pmatrix}\delta u_{\mathbf{k}}\\ \delta w_{\mathbf{k}}\end{pmatrix}\exp(-i\mathbf{k}\cdot\mathbf{r}), \qquad (29)$$

$$\delta T=\delta T_{\mathbf{k}}\exp(-i\mathbf{k}\cdot\mathbf{r}). \qquad (30)$$

With this choice the resulting equations have the form

$$\begin{pmatrix}\partial_t\delta\rho_{\mathbf{k}}\\ \partial_t\delta u_{\mathbf{k}}\\ \partial_t\delta w_{\mathbf{k}}\\ \partial_t\delta T_{\mathbf{k}}\end{pmatrix}=-\mathbf{A}\begin{pmatrix}\delta\rho_{\mathbf{k}}\\ \delta u_{\mathbf{k}}\\ \delta w_{\mathbf{k}}\\ \delta T_{\mathbf{k}}\end{pmatrix}, \qquad (31)$$

where **A** is the stability matrix with elements given in the Appendix.

With the help of MAPLE V release 5 we analyzed the eigenvalues of the stability matrix **A** for different densities, restitution coefficients, wave numbers, and sites. In Figs. 4–7 we present results for some of the parameter sets that are representative for the different situations. With the choice of the negative sign in Eq. (31) a negative eigenvalue means an unstable solution. All of the figures shown feature at least one eigenvalue that is negative in the small wave number region. This signalizes an unstable fluctuation. The upper zero point of this eigenvalue approaches the zero wave number as we increase the restitution coefficient and becomes smaller than $2\pi/L$, the smallest possible wave number in the system, at a certain value of e_n that depends on the other parameters. However, this value is very close to 1, which suggests that the symmetrical solution is always unstable linearly, and nonlinear effects can move this transition point to higher inelasticities. We analyzed the most unstable direction of the solution also, as we plotted the unstable eigenvalue for a given amplitude of the wave number and for the whole angle measured from the direction of the mean flow in a counterclockwise direction, as seen in Figs. 8 and 9. According to the figures, the most unstable directions are close to

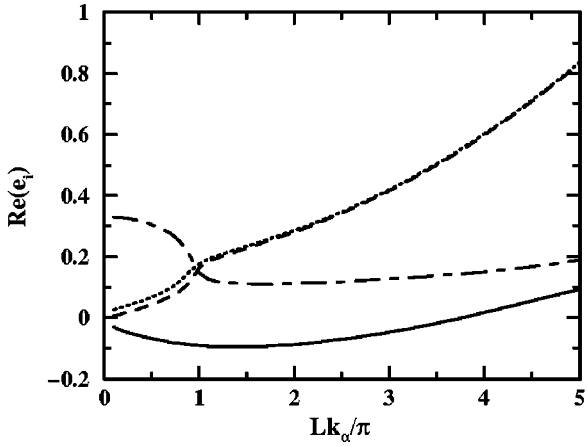

FIG. 4. Eigenvalues of the stability matrix for $e_n = 0.9$, $y = 0$, average packing fraction $\overline{\nu} = 0.486$, and $\mathbf{k}_\alpha$ points in the direction $\alpha = \pi/4$ measured counterclockwise from the mean flow direction.

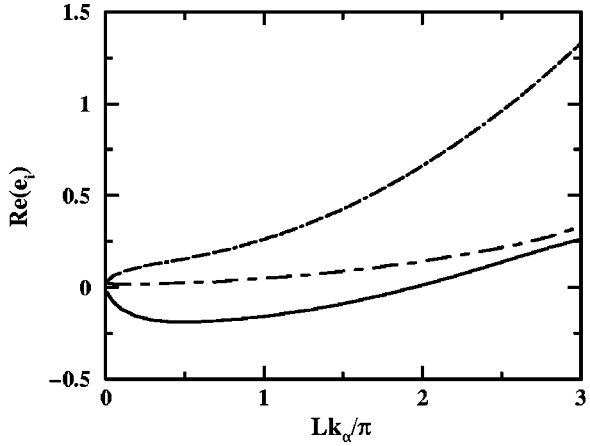

FIG. 6. Eigenvalues of the stability matrix for $e_n = 0.997$, $y = 0$, average packing fraction $\overline{\nu} = 0.486$, and $\mathbf{k}_\alpha$ points in the direction $\alpha = \pi/4$ measured counterclockwise from the mean flow direction.

the angles ± $\pi/4$. These are the same angles found to be the governing unstable directions in linear order for pattern formation by Tan and Goldhirsch for the uniformly sheared granular gas [8].

IV. SELF-DIFFUSION COEFFICIENT AND CLUSTERED FLOWS

In this section we investigate the crossover to asymmetric stationary states of the system and try to show the effect of the instability discussed above on the transport coefficients. For this reason we measured the mean square displacement of the particles

$$r_x^2 = \langle [x(t) - \langle v_x \rangle t - x(0)]^2 \rangle, \quad r_y^2 = \langle [y(t) - y(0)]^2 \rangle \tag{32}$$

and velocity correlation functions

$$c_x = \langle [v_x(t) - \langle v_x \rangle][v_x(0) - \langle v_x \rangle] \rangle, \quad c_y = \langle v_y(t) v_y(0) \rangle \tag{33}$$

in the system for streamwise and perpendicular directions. In Eqs. (32) and (33) the brackets $\langle \rangle$ mean space and ensemble averages over the whole system. $\langle v_x \rangle$ was calculated from the measured average displacement of the particles averaged over several (50–100) runs and over particles. Ensemble averages were carried out the following way. For every parameter set we let the system relax to its steady state. The measured granular temperature averaged over stripes of width $1 = r$ generated the $T(y)$ function. Before every measurement we perturbed the velocities of every particle with a uniformly distributed velocity, the support of the distribution having the length of $2\sqrt{T(y)}$, where y is the coordinate of the particle. After relaxation we carried out the measurement. The $\langle v_x \rangle$ average velocity was evaluated from a linear fit of the averaged x displacement of the particles, that is, the steepness of x as a function of time.

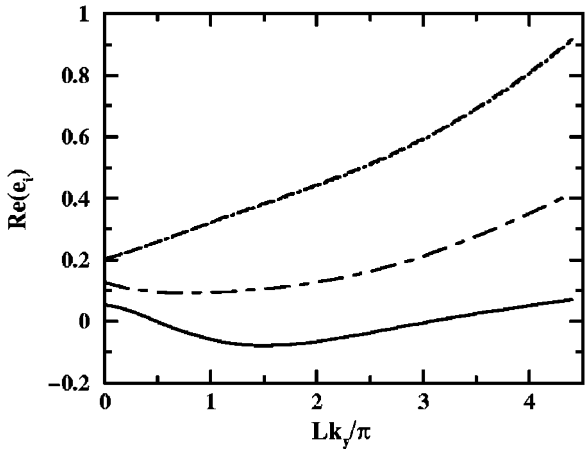

FIG. 5. Eigenvalues of the stability matrix for $e_n = 0.95$, $y = 0$, $k_x = 2\pi/L$, and average packing fraction $\overline{\nu} = 0.486$ as a function of $k_y L/\pi$.

From the mean square displacement for long times we could evaluate the diffusion coefficient of the particles. We fitted a power law with two fit parameters D and b,

$$f(t) = 2Dt^b,$$

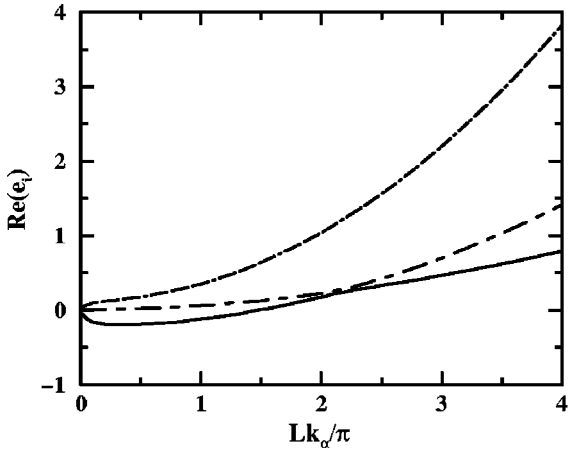

FIG. 7. Eigenvalues of the stability matrix for $e_n = 0.999$, $y = 0$, average packing fraction $\overline{\nu} = 0.486$, and $\mathbf{k}_\alpha$ points in the direction $\alpha = \pi/4$ measured counterclockwise from the mean flow direction.

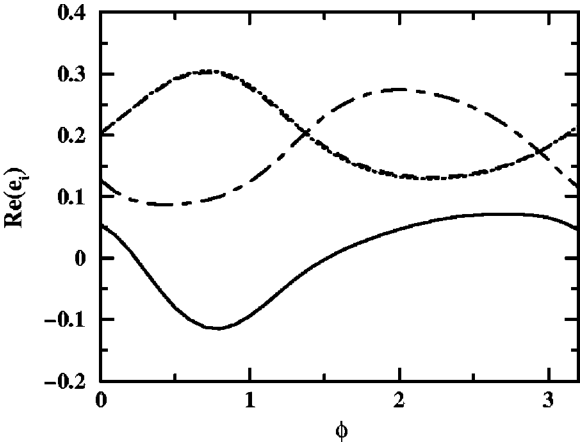

FIG. 8. Angle dependence of the real part of the eigenvalues for $e_n=0.95$, $y=0$, and $\overline{\nu}=0.486$. The eigenvalue is plotted as a function of the angle measured from the flow direction $k_x=(2\pi/L)\cos(\phi)$ and $k_y=(2\pi/L)\sin(\phi)$.

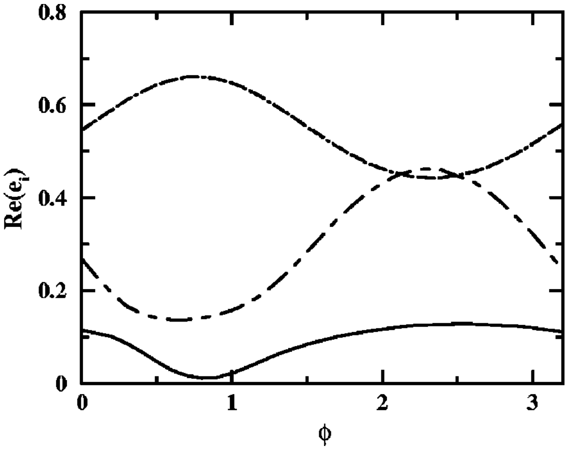

FIG. 9. Angle dependence of the real part of the eigenvalue for $e_n=0.997$, $y=0$, and $\overline{\nu}=0.486$. The eigenvalue is plotted as a function of the angle measured from the flow direction $k_x=(2\pi/L)\cos(\phi)$ and $k_y=(2\pi/L)\sin(\phi)$.

to the mean square displacement restricted to long times. If the value of b was near 1 up to errors of ± 0.02, the system was assumed to be in a diffusive state. After that we took $b=1$ and fitted $f(t)$ again for D. The time taken for the system to evolve into this diffusive state depends on e_n, as suggested in [20] for the homogeneous cooling state, and also depends on the steady state configuration, which is also e_n dependent. There are several reasons for this. First, to achieve this diffusive behavior in the x direction the particles have to experience the characteristics of the system—finiteness and inhomogeneity of the hydrodynamic profiles—and therefore have to travel between the two walls several times. As e_n decreases and a dense cluster evolves at one wall, this recognition takes more and more time. Also, the form of the velocity correlation function shows increasing correlations with decreasing e_n, as expected. After a short ($t\approx 10$) fast decay, c_x shows an exponential decay up to times $t\approx 100$, and either changes to a slow decay for later times (small e_n) or is relaxed (large e_n) (Fig. 10). Both the short time correlations and the characteristic time of the exponential increase as we decrease e_n, along with an earlier changeover to the slow decay if it is apparent.

The plot of the diffusion coefficient versus restitution coefficient (Fig. 11) shows a plateau value of the diffusion coefficient for larger values of e_n. Below $e_c=0.82$, D increases fast with decreasing e_n. We suggest that this value marks the transition point where the particles begin to prefer one of the walls, and the dilute regions appearing allow for a greater mobility for the particles. Making use of the noted exponential decay of the velocity autocorrelation c_x, we also estimated D as the integral of a fitted exponential,

$$D\approx A\tau \quad \text{if} \quad c_x\approx Ae^{-t/\tau},$$

knowing that this underestimates D, as $Ae^{-t/\tau}$ is smaller than c_x for very short and long times, but gives nearly the same result as the long time behavior of r_x^2 above the transition point and shows a smaller increase below it (Fig. 11). The difference between the values of the diffusion coefficient below e_c, obtained with different methods, comes from the fact that under the transition point there appears a slow decay in the velocity correlation function after the exponential decay used to approximate it. The short time exponential decay characterizes only the dilute part of the system. The slow decay thereafter comes from the averaged effects of the slight diffusion in the dense region and from the influence of particles entrapped or emitted by the dense region from or to the dilute one. In the absence of the asymmetric dense state above the transition point e_c, only the exponential relaxation appears.

The buildup of correlations also causes increased time to be needed to reach the diffusive state, thus increasing simulation time, which restricted us to smaller system sizes for dense material, as it did not allow fast computations. Therefore the investigation of the size and density dependence of the transition point is left for later studies.

The retrievable information from the mean square displacement in the y direction is bounded like the system itself, namely, it goes to a plateau value according to L_y. This finiteness influences velocity correlations also. c_y shows only short time fast decaying correlations (and anticorrelations appear for small e_n). With the methods discussed above we do not notice any mark of the transition (only the small signal presented in [21] for time-step-driven simulations).

For more definite insight into the behavior of the system, we carried out measurements specific to the configuration of the stationary states. We divided the system into stripes parallel to the walls and restricted the averages in Eq. (33) to particles starting from these stripes,

$$c_x^i=\langle[v_x(t)-\overline{v_x^i}(t)][v_x(0)-\overline{v_x^i}(0)]\rangle_i,$$

$$c_y^i=\langle v_y(t)v_y(0)\rangle_i, \tag{34}$$

where $\langle\ \rangle_i$ denotes averaging over particles in stripe i at $t=0$ and the ensemble average described above. The velocity $\overline{v_x^i}(t)$ is the average velocity of particles starting from stripe i at time t. This velocity correlation function characterizes the stripe more and more as the difficulty in leaving the stripe increases, which is the case in the dense layer evolving at the wall. The fact that the velocity correlation function c_x^i

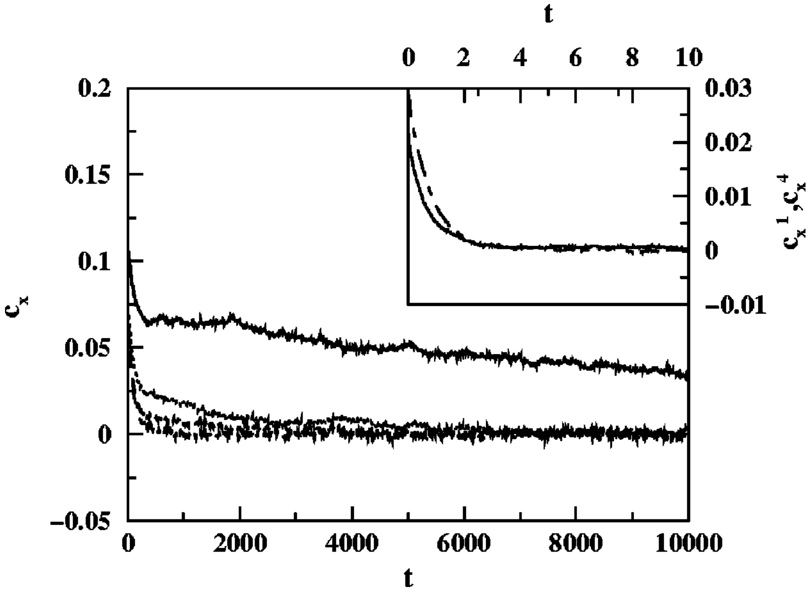

FIG. 10. Velocity autocorrelation functions c_x (in units of $U^2=25$) for a system with parameters $L_x=20$, $L_y=20$, and $N=50$ ($\overline{\nu}=0.426$). In order of increasing c_x for short times are $e_n=0.8, 0.78, 0.77, 0.76$. Inset: Velocity autocorrelation functions c_x^i (same units) for a system $L_x=80$, $L_y=20$, $N=200$ ($\overline{\nu}=0.426$), and $e=0.76$. The system was divided into five stripes of width 4. Only correlation functions in the stripes at the walls are shown. Solid line marks the function at the wall of the cluster, and dot-dashed line at the opposite wall. Time is measured in natural units ($r=1, U=5$).

does not show a negative minimum at short times (Fig. 10)—which would be a sign of caging effects—suggests that the particles essentially comoving with the wall barely move in the x direction with respect to one another. Instead, because of the shear situation, they are driven by diagonal collisions which dominate the motion and smooth out c_x. There is a negative minimum in c_y^0 (0 indexing the stripe nearest to the wall at the cluster) but this includes the effect of the collisions with the wall particles, which give a negative contribution, as also seen in the velocity correlations in the stripe at the opposite wall. This negative minimum appears also at restitution coefficients well above the transition.

V. DISCUSSION

In this paper we considered a granular gas sheared by two bumpy walls. By means of molecular dynamics simulations we discovered that the system shows a spontaneous symmetry breaking as it evolves to a stationary state that is asymmetric in the hydrodynamic fields with respect to the centerline of the system. The location to which this density maximum (temperature minimum) is shifted from the symmetry axes is predetermined by the initial velocity distribution, as the system chooses the wall according to this distribution, as discussed in Sec. II. During the simulations, measuring the mean y coordinate of the particles, we did not observe any switch between the possible two states where the asymmetry was explicit. We found in a linear stability analysis that the symmetrical solution proposed by Jenkins and Richman [12] is unstable. In analyzing the solution [12] one finds that the description of the asymmetric profiles needs higher order equations in ϵ than in [12]. We do not consider this analysis as a strict result quantitatively. According to [22] the equations of Jenkins and Richman are not suitable for linear stability analysis because they neglect the time dependence of the mean free path. But the equations with the corrected constitutive relations [10] have the same dependence on the hydrodynamic field and differ in the e_n dependence only. We assume that this correction term cannot stabilize the system but can at most increase the e_n value under which the solution becomes unstable.

We found a connection to the unstable directions observed in uniformly sheared granular gases [8]. This suggests that nonuniformly sheared systems possess the same instability but in the Couette case the pattern formation is repressed by the boundary conditions. However, the geometry of the boundary conditions (walls) plays a major role in stabilizing

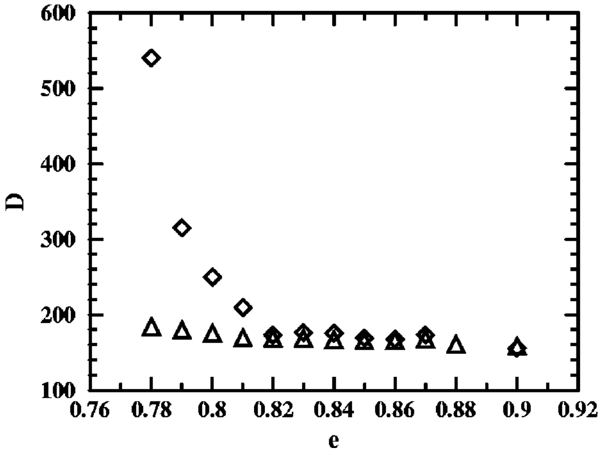

FIG. 11. The self-diffusion coefficient as a function of the restitution coefficient e_n for $L_x=L_y=20$, and $N=50$ ($\overline{\nu}=0.426$) measured in natural units. These runs were carried out by moving both walls in opposite directions with $U=\pm 5$. Diamonds (◇) mark values determined from the mean square displacement, and triangles (△) mark values determined from the velocity autocorrelation function.

the flow fields, leading to a stationary state. In the boundary conditions of Jenkins and Richman [12] only static correlations are considered and dynamic correlations, the role of multiple and correlated recollisions with the wall, are neglected. We measured the number of collision sequences, which consist of collisions of a disk with two wall disks successively, because such collisions provide disks leaving the wall at a steeper angle, and this can provide a greater contribution to the pressure at lower granular temperatures. In the asymmetric flow regime, the number of such collisions is clearly higher at the preferred wall than at the other, which supports our assumption. This is also implied by the fact that in the final stationary state the minimum of the granular temperature is only at the wall for very high inelasticities or densities, where we can observe closed layers of particles at the chosen wall. For moderate densities and restitution, the temperature minimum remains in the bulk of the system, and the clustering process stops at a stable density profile. Such an effect was described for a constrained homogeneous system in [5]. These boundary effects are one reason for the different results for the transition point obtained from stability analysis or from measurement of the self-diffusion coefficient and velocity autocorrelation functions. The effect found in the dependency of these functions on the normal restitution coefficient (see Sec. IV) is well described as a consequence of the transition. However, the system size used in the simulations is too small to compare the two results. We suggest that for larger systems where the Jenkins-Richman theory is more valid we would obtain larger values for the transition point but we leave the measurements involved for later studies. As a final note we would like to mention that, in systems with elastic collisions with the wall disks, the flow with the same parameters remains symmetric.

The consequences of this paper are hard to verify in experiments because of the absence of gravity. However, microgravity experiments for the same configuration are under way [23]. We suggest that the two-dimensional case considered here would be realizable with disks on an air table, as this would exclude gravity effects and would not interfere with the behavior of the disks in the crucial horizontal direction. Periodic boundary conditions could be achieved with two similar stadionlike chains of disks, as performed in [23].

ACKNOWLEDGMENTS

M.S. (J.K.) wishes to acknowledge the financial help of the DAAD (AvH Foundation). This work was partially supported by Grant Nos. OTKA T029985 and OTKA T024004.

APPENDIX: THE LINEAR STABILITY MATRIX

In the following we describe the matrix elements of the linear stability matrix. The notations include $\rho = \vartheta\nu$ where $\vartheta = \pi/4$ for $\sigma = 1$, $m = 1$, and $\varphi = \partial_y[\nu g_0(\nu)]$

$$A_{11} = uik_x; \tag{A1}$$

$$A_{12} = \rho ik_x; \tag{A2}$$

$$A_{13} = \rho ik_y + \partial_y\rho; \tag{A3}$$

$$A_{14} = 0; \tag{A4}$$

$$\begin{aligned} A_{21} = {} & 2T\varphi ik_x + \frac{2\nu g_0 Tik_x}{\rho} - \frac{\sigma}{\sqrt{\pi}}\partial_y^2 u\left(\frac{\nu g_0\sqrt{T}}{\rho} + \sqrt{T}\varphi\vartheta\right) \\ & - \frac{\sigma}{\sqrt{\pi}}\frac{\partial_y u}{\rho}\left[\varphi\sqrt{T} + \nu g_0\left(\frac{\partial_y T}{2\sqrt{T}} + \sqrt{T}ik_y\right) + \partial_y\rho\sqrt{T}\varphi\vartheta\right] \\ & - \frac{\sigma}{\sqrt{\pi}}\partial_y u\vartheta\left(\frac{\partial_y T\varphi}{2\sqrt{T}} + \sqrt{T}\partial_y\varphi + \sqrt{T}\varphi ik_y\right); \end{aligned} \tag{A5}$$

$$\begin{aligned} A_{22} = {} & uik_x + \frac{\sigma\nu g_0\sqrt{T}}{\sqrt{\pi}}\left[3k_x^2 + k_y^2 - \left(\frac{\partial_y\rho}{\rho} + \frac{\partial_y T}{2T}\right)ik_y\right] \\ & - \frac{\sigma}{\sqrt{\pi}}\varphi\sqrt{T}ik_y; \end{aligned} \tag{A6}$$

$$\begin{aligned} A_{23} = {} & \partial_y u + \frac{\sigma\nu g_0\sqrt{T}}{\sqrt{\pi}} \\ & \times\left[2k_xk_y - \left(\frac{\partial_y\rho}{\rho} + \frac{\partial_y T}{2T}\right)ik_x\right] - \frac{\sigma}{\sqrt{\pi}}\varphi\sqrt{T}ik_x; \end{aligned} \tag{A7}$$

$$\begin{aligned} A_{24} = {} & 2\nu g_0 ik_x - \frac{\sigma\nu g_0\partial_y^2 u}{2\sqrt{T\pi}} - \frac{\sigma\partial_y^2 u}{2\sqrt{T\pi}} \\ & \times\left[\varphi + \nu g_0\left(\frac{\partial_y\rho}{\rho} - \frac{\partial_y T}{2T} + ik_y\right)\right]; \end{aligned} \tag{A8}$$

$$\begin{aligned} A_{31} = {} & 2\left(\frac{\partial_y\rho T\varphi}{\rho} + \partial_y T\varphi + T\partial_y\varphi\right)\vartheta + 2T\varphi\vartheta ik_y \\ & + \frac{2\varphi T}{\rho} + 2\frac{\nu g_0}{\rho}(\partial_y T + Tik_y) \\ & - \frac{\sigma\partial_y u}{\sqrt{\pi}}\left(\frac{\nu g_0\sqrt{T}ik_x}{\rho} + \sqrt{T}\varphi ik_x\vartheta\right); \end{aligned} \tag{A9}$$

$$A_{32} = \frac{\sigma\nu g_0\sqrt{T}}{\sqrt{\pi}}\left[2k_xk_y - \left(\frac{\partial_y\rho}{\rho} + \frac{\partial_y T}{2T}\right)ik_x\right] - \frac{\sigma}{\sqrt{\pi}}\varphi\sqrt{T}ik_x; \tag{A10}$$

$$\begin{aligned} A_{33} = {} & uik_x + \frac{\sigma\nu g_0\sqrt{T}}{\sqrt{\pi}}\left[k_x^2 + 3k_y^2 - \left(\frac{\partial_y\rho}{\rho} + \frac{\partial_y T}{2T}\right)3ik_y\right] \\ & - \frac{\sigma}{\sqrt{\pi}}\varphi\sqrt{T}3ik_y; \end{aligned} \tag{A11}$$

$$A_{34} = 2\nu g_0\left(\frac{\partial_y\rho}{\rho} + ik_y\right) + 2\varphi - \frac{\sigma\nu g_0\partial_y uik_x}{2\sqrt{t\pi}}; \tag{A12}$$

$$\begin{aligned}A_{41}=&\left(\frac{8(1-e_n)}{\sigma\sqrt{\pi}}T^{3/2}-\frac{2\sigma\sqrt{T}\partial_y^2T}{\sqrt{\pi}}\right)\left(\frac{\nu g_0}{\rho}+\varphi\vartheta\right)\\&-\frac{2\sigma\partial_yT}{\sqrt{\pi}\rho}\left[\varphi\sqrt{T}+\nu g_0\left(\frac{\partial_yT}{2\sqrt{T}}+\sqrt{T}ik_y\right)+\varphi\partial_y\rho\sqrt{T}\vartheta\right]\\&-\frac{2\sigma\partial_yT\vartheta}{\sqrt{\pi}}\left(\partial_\varphi\sqrt{T}+\frac{\varphi\partial_yT}{2\sqrt{T}}+\varphi\sqrt{T}ik_y\right)\\&-\frac{\sigma\sqrt{T}}{\sqrt{\pi}}(\partial_u)^2\left(\frac{\nu g_0}{\rho}+\varphi\vartheta\right);\end{aligned}\tag{A13}$$

$$A_{42}=2\nu g_0Tik_x-\frac{2\sigma}{\sqrt{\pi}}\nu g_0\sqrt{T}\partial_yuik_y;\tag{A14}$$

$$A_{43}=\partial_yT+2\nu g_0Tik_y-\frac{2\sigma}{\sqrt{\pi}}\nu g_0\sqrt{T}\partial_yuik_x;\tag{A15}$$

$$\begin{aligned}A_{44}=&uik_x+\frac{12(1-e_n)\nu g_0\sqrt{T}}{\sigma\sqrt{\pi}}+\frac{2\sigma\nu g_0\sqrt{T}}{\sqrt{\pi}}\\&\times\left[k_x^2+k_y^2-\left(\frac{\partial_y\rho}{\rho}+\frac{\partial_yT}{2T}\right)ik_y\right]\\&-\frac{2\sigma}{\sqrt{\pi}}\varphi\sqrt{T}ik_y-\frac{\sigma\nu g_0}{\sqrt{T\pi}}\partial_y^2T-\frac{\sigma}{\sqrt{T\pi}}\partial_yT\\&\times\left[\varphi+\nu g_0\left(\frac{\partial_y\rho}{\rho}-\frac{\partial_yT}{2T}\right)+\nu g_0ik_y\right]-\frac{\sigma\nu g_0}{2\sqrt{T\pi}}(\partial_yu)^2.\end{aligned}\tag{A16}$$

---

[1] I. Goldhirsch and G. Zanetti, Phys. Rev. Lett. **70**, 1619 (1993).

[2] S. McNamara, Phys. Fluids A **5**, 3056 (1993).

[3] J.J. Brey, M.J. Ruiz-Montero, and F. Moreno, Phys. Fluids **10**, 2976 (1998).

[4] T.P.C. van Noije and M.H. Ernst, Phys. Rev. E **61**, 1765 (2000).

[5] J.J. Brey, R.J. Ruiz-Montero, and D. Cubero, Phys. Rev. E **60**, 3150 (1999).

[6] R. Brito and M.H. Ernst, Europhys. Lett. **43**, 497 (1998).

[7] J.T. Jenkins, J. Appl. Mech. **59**, 120 (1992).

[8] M-L. Tan and I. Goldhirsch, Phys. Fluids **9**, 856 (1997).

[9] N. Sela, I. Goldhirsch, and S.H. Noskovitz, Phys. Fluids **8**, 2337 (1996).

[10] N. Sela and I. Goldhirsch, J. Fluid Mech. **361**, 41 (1998).

[11] M-L. Tan and I. Goldhirsch, Phys. Rev. Lett. **81**, 3022 (1998).

[12] J.T. Jenkins and M.W. Richman, J. Fluid Mech. **171**, 53 (1986).

[13] J.T. Jenkins and M.W. Richman, Phys. Fluids **28**, 3485 (1985).

[14] M.W. Richman and C.S. Chou, ZAMP **39**, 885 (1988).

[15] D. E. Wolf, in *Computational Physics*, edited by K.H. Hoffmann and M. Schreiber (Springer, Heidelberg, 1996).

[16] S. McNamara and W.R. Young, Phys. Rev. E **50**, R28 (1994); **53**, 5089 (1996).

[17] M. Sasvári, J. Kertész, and D.E. Wolf, in *Traffic and Granular Flow '97*, edited by M. Schreckenberg and D.E. Wolf (Springer, Singapore, 1998).

[18] J.J. Brey, J.W. Dufty, C.S. Kim, and A. Santos, Phys. Rev. E **58**, 4638 (1998).

[19] V. Garzó and J.W. Dufty, Phys. Rev. E **59**, 5895 (1999).

[20] J.J. Brey, M.J. Ruiz-Montero, D. Cubero, and R. Garcia-Rojo, Phys. Fluids **12**, 876 (2000).

[21] M. Sasvári, J. Kertész, and D.E. Wolf, in *Anomalous Diffusion: From Basics to Applications*, Vol. 519 of *Lecture Notes in Physics*, edited by A. Pekalski and K. Sznajd-Weron (Springer, Berlin, 1999), pp. 349–357.

[22] I. Goldhirsch, Chaos **9**, 659 (1999).

[23] M.Y. Louge and J.T. Jenkins (unpublished).